Nematic Electronic Structure in the "Parent" State of the Iron-Based Superconductor $Ca(Fe_{1-x}Co_x)_2As_2$

T.-M. Chuang,[1,2]* M. P. Allan,[1,3]* Jinho Lee,[1,4] Yang Xie,[1] Ni Ni,[5,6] S. L. Bud'ko,[5,6] G. S. Boebinger,[2] P. C. Canfield,[5,6] J. C. Davis[1,3,4,7]†

The mechanism of high-temperature superconductivity in the newly discovered iron-based superconductors is unresolved. We use spectroscopic imaging–scanning tunneling microscopy to study the electronic structure of a representative compound $CaFe_{1.94}Co_{0.06}As_2$ in the "parent" state from which this superconductivity emerges. Static, unidirectional electronic nanostructures of dimension eight times the inter–iron-atom distance $a_{Fe\text{-}Fe}$ and aligned along the crystal a axis are observed. In contrast, the delocalized electronic states detectable by quasiparticle interference imaging are dispersive along the b axis only and are consistent with a nematic α_2 band with an apparent band folding having wave vector $\vec{\mathbf{q}} \cong \pm 2\pi/8a_{Fe\text{-}Fe}$ along the a axis. All these effects rotate through 90 degrees at orthorhombic twin boundaries, indicating that they are bulk properties. As none of these phenomena are expected merely due to crystal symmetry, underdoped ferropnictides may exhibit a more complex electronic nematic state than originally expected.

The ferropnictide (*1*–*6*) and cuprate high-temperature superconductors exhibit several apparent similarities. These include, for example, commensurate antiferromagnetism (AF) in the parent compounds, the quasi–two-dimensional nature of the CuO_2 and FeAs superconducting planes, and the importance of the transition-metal–atom d states. One consequence of strong electronic correlations in the cuprates is the potential for smectic ("striped") or nematic electronic liquid crystal states (*7*–*10*). Neutron scattering provides clear evidence for magnetic "stripes" in some cuprates (*10*), whereas spectroscopic imaging–scanning tunneling microscopy (SI-STM) provides imaging evidence for electronic nematicity in the cuprate "pseudogap" states (*11*, *12*). There are proposals that such electronic phenomena may be critical to high-temperature superconductivity in cuprates (*9*, *10*). If similar phenomena existed in the parent state of ferropnictides, it could alter perceptions of the potential mechanism of high-temperature superconductivity in those systems.

Members of the $AEFe_2As_2$ (where AE = Ca, Sr, or Ba) ferropnictide family typically exhibit a phase diagram as shown in Fig. 1A. Doping is achieved by either cation substitution outside the FeAs layer or transition-metal–atom substitution within this layer. The parent compounds are antiferromagnetic with a phase-transition temperature T_{AF} between 134 and 220 K (*13*). T_{AF} diminishes with increasing doping (blue curve), and the superconductivity occurs within a "dome" (green curve). The antiferromagnetic transition is always intertwined with a structural transition from tetragonal to orthorhombic crystal symmetry (Fig. 1A). The a axis unit cell length becomes typically ~1% longer than that of the b axis at temperature T_S, just above (or at) the antiferromagnetic transition (red curve). In this unusual AF state, each Fe atom along the b axis has parallel spins, whereas those aligned along the a axis have antiparallel spins (Fig. 1A). Inelastic neutron scattering studies show that the magnetic excitation structure can exhibit strong 180° (C_2) symmetry such that nearest-neighbor exchange constants along the a and b axes, J_{1a} and J_{1b}, are dramatically different in magnitude (*14*, *15*), despite such minute lattice distortions.

This combination of commensurate AF with a tiny periodic moment, large exchange anisotropy with minute orthorhombic lattice distortion, and a high T_{AF} for such an antiferromagnetic state has motivated a search for new explanations for the phases and magnetic phenomenology of underdoped ferropnictides. A plausible account of the underdoped magnetic ground state can be found in local spin models (*16*–*18*). Yet even within such relatively simple pictures of the magnetism, unidirectional magnetic nanodomains, separated by magnetic twin or antiphase boundaries (*19*), should exist. Electronic nematicity is anticipated because of the orthorhombic crystal symmetry (*18*, *20*). Moreover, functional renormalization group theory shows that a Pomeranchuk instability toward a C_2 symmetry nematic electronic structure is possible (*21*). A microscopic proposal to explain the simultaneous lattice and magnetic phase transitions and all of their peculiarities is that nematic orbital-ordering occurs in the d_{xz} and d_{yz} orbitals of Fe (*22*–*25*).

Thus, our objective is to examine the spatial arrangements in the electronic structure of the parent state of ferropnictides by imaging simultaneously their real space ($\vec{\mathbf{r}}$-space) and momentum space ($\vec{\mathbf{k}}$-space) electronic characteristics. SI-STM can be a powerful technique to achieve such electronic structure imaging; it has already revealed the structure and arrangement of ferropnictide vortices (*26*). Measurement of the STM tip-sample differential tunneling conductance $dI/dV(\vec{\mathbf{r}},V) \equiv g(\vec{\mathbf{r}},E=eV)$ at locations $\vec{\mathbf{r}}$ and sample-bias voltage V (here, E is the electron energy, and e is a single electron charge) yields an image proportional to the local density of electronic states $LDOS(\vec{\mathbf{r}},E)$. Elements of the $\vec{\mathbf{k}}$-space electronic structure can then be determined by using Fourier transform scanning tunneling spectroscopy, because the spatial modulations in $g(\vec{\mathbf{r}},E)$ due to scattering interference of quasiparticles are detectable in $g(\vec{\mathbf{q}},E)$, which is the Fourier transform of $g(\vec{\mathbf{r}},E)$ (here, $\vec{\mathbf{q}}$ is the wave vector reciprocal to $\vec{\mathbf{r}}$).

However, the poor morphology of the cleaved surface of many ferropnictides (*27*–*31*) has made it challenging to achieve large–field-of-view (FOV), atomically registered $g(\vec{\mathbf{r}},E)$ imaging that is necessary to examine the FeAs-layer electronic structure with SI-STM. To avoid such cleave-surface pathologies, we explored the cryo-cleave characteristics of several different ferropnictide 122 compounds and eventually discovered that $Ca(Fe_{1-x}Co_x)_2As_2$ can be cleaved to reveal large, perfectly flat, debris-free and stable surfaces with excellent atomic resolution (Fig. 1B).

$Ca(Fe_{1-x}Co_x)_2As_2$ is well-representative of the ferropnictide 122 compounds (*6*, *32*–*34*). $CaFe_2As_2$ exhibits simultaneous structural and magnetic phase transitions (*32*, *33*) at 170 K. Angle-resolved photoemission spectroscopy (ARPES) reveals its Fermi surface arrangement in good agreement with reports from related compounds (*34*), and inelastic neutron scattering detects the reduction of symmetry in the magnetic excitation spectrum to C_2 (*14*, *15*). These observations make $Ca(Fe_{1-x}Co_x)_2As_2$ an excellent material in which to explore the nematic electronic structure of the underdoped ferropnictide state that is "parent" to the superconductivity.

For this study, we used $Ca(Fe_{1-x}Co_x)_2As_2$ samples with $x \sim 3.0 \pm 0.5\%$. The samples were inserted into the SI-STM system and cleaved in cryogenic ultrahigh vacuum; all data were acquired at 4.3 K. Figure 1B shows the typical surface conditions achieved in our experiments. This ~71-nm square FOV is believed to be the As-terminated FeAs plane (*30*, *31*) with an unknown distribution of Ca atoms (and, thus, an unknown degree of charge transfer at that plane). The plane is atomically flat but with a 1 × 2 surface reconstruction (blue and red arrows in Fig. 1B inset) at ~45° to both the a and b axes. The inset to Fig. 1B is a 4.2-nm square topograph

[1]Laboratory of Atomic and Solid State Physics, Department of Physics, Cornell University, Ithaca, NY 14853, USA. [2]National High Magnetic Field Laboratory, Department of Physics, Florida State University, Tallahassee, FL 32310, USA. [3]School of Physics and Astronomy, University of Saint Andrews, Saint Andrews, Fife KY16 9SS, UK. [4]Condensed Matter Physics and Materials Science Department, Brookhaven National Laboratory, Upton, NY 11973, USA. [5]Ames Laboratory, U.S. Department of Energy (DOE), Iowa State University, Ames, IA 50011, USA. [6]Department of Physics and Astronomy, Iowa State University, Ames, IA 50011, USA. [7]Department of Physics and Astronomy, University of British Columbia, Vancouver, British Columbia, Canada.

*These authors contributed equally to this work.
†To whom correspondence should be addressed. E-mail: jcdavis@ccmr.cornell.edu

of this surface in which the individual atoms on the reconstruction rows can be seen (red arrows). This 1 × 2 reconstruction is not a bulk property (*27*, *29*, *31*) but rather a surface condition whose effects must be avoided in SI-STM studies of the FeAs-plane electronic structure. In our studies, the orientation of the orthorhombic *a* and *b* axes can be determined from the topography (figs. S1 and S2).

Detailed examination of high-quality topographs of these surfaces reveals the first surprising fact. Figure 1B is typical; it appears to show faint unidirectional structures aligned along the *a* axis (orange arrows). Figure 2A shows that, when two identical atomically registered topographs measured at ±50 meV are subtracted (to cancel the signals of the surface reconstruction and topographic disorder that are independent of the sign of the tunnel bias), unidirectional nanostructures aligned along the *a* axis are seen. Because topographs represent a logarithmic measure of the integrated density of states, these data indicate the existence of some form of static electronic nanostructure. To get a clearer picture of any such electronic nanostructures, we image the energy-resolved $LDOS(\vec{\mathbf{r}},E)$ in the same FOV (fig. S3). Remarkably, electronic nanostructures aligned with the *a* axis and spatially equivalent to those in Fig. 2A are detected in all low-energy $LDOS(\vec{\mathbf{r}},E)$ images (fig. S3). To determine if these phenomena indicate static or dispersive states, one must integrate the $LDOS(\vec{\mathbf{r}},E)$ over energy. Thus, we image directly the net tunnel current *I* because

$$I(\vec{\mathbf{r}},E) = \int_0^E g(\vec{\mathbf{r}},E')dE' \qquad (1)$$

Figure 2B is an image of $I(\vec{\mathbf{r}},E = 50\ \text{meV})$; it reveals the same electronic nanostructures and thereby demonstrates that they must be static over this energy range. Moreover, autocorrelation analysis of such images (Fig. 2, A and B, insets) shows that the static structures throughout the image are all aligned with the *a* axis and are self-similar with a characteristic dimension of eight inter–iron-atom distances, ~$8a_{\text{Fe-Fe}}$. The spatially averaged density-of-states $DOS(E)$ spectrum (Fig. 2C, inset) consists of a metallic density-of-

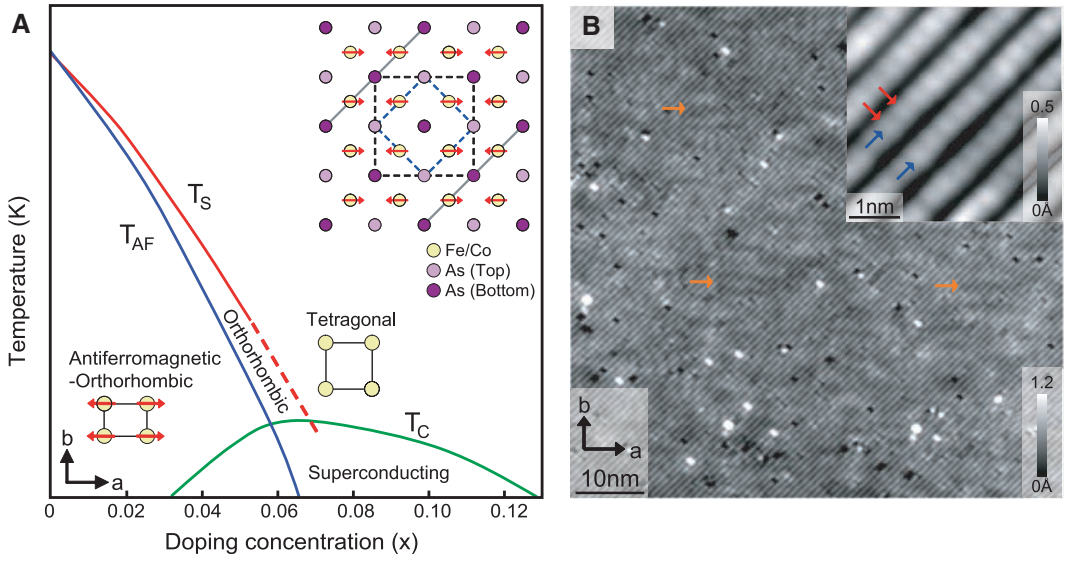

Fig. 1. (**A**) Schematic phase diagram of $AE(Fe_{1-x}Co_x)_2As_2$ (here *AE* = Ca, Sr, or Ba) as function of doping concentration (*x*) (*6*, *13*, *32*, *33*). Red, blue, and green curves show the transition temperature for structure (T_S), antiferromagnetism (T_{AF}), and superconductivity (T_C), respectively. The red arrows indicate the spin orientation for each Fe atom in the antiferromagnetic-orthorhombic phase. (Upper right) FeAs layer showing the unit cell in tetragonal (blue dashed lines) and orthorhombic (black dashed lines) phases. The orientation and periodicity of the surface reconstruction in the topographic images in (B) is indicated by gray lines. (**B**) Constant-current topographic image of $Ca(Fe_{1-x}Co_x)_2As_2$ taken at $V_0 = -50$ mV and $I_z = 10$ pA on a 71.0-nm square FOV. (Inset) A high-resolution topograph in a smaller FOV (4.2-nm square) taken at $V_0 = -5$ mV and $I_z = 100$ pA. The red and blue arrows indicate the atoms of 1 × 2 configuration. The orange arrows indicate the first indications of unidirectional *a* axis–oriented electronic nanostructures.

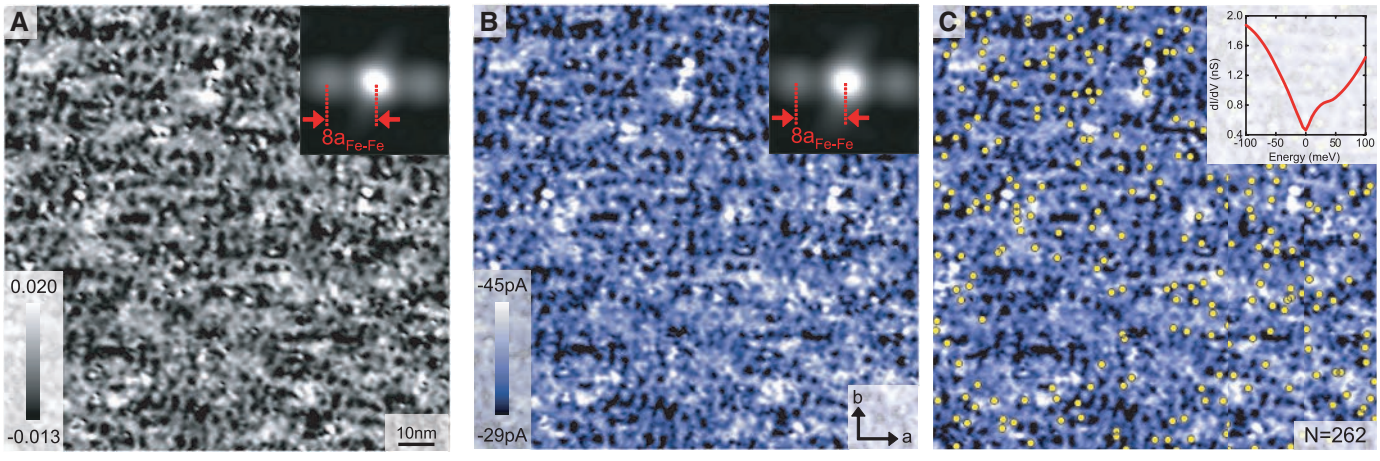

Fig. 2. (**A**) Difference between two atomically registered topographs *z*(+50 mV) − *z*(−50 mV) (where *z* is the tip-sample distance), acquired in the same 61.3-nm square FOV at I_z = 10 pA. (Inset) Autocorrelation analysis of this image; the centers of self-similarity peaks (red dotted lines) are separated by ~$8a_{\text{Fe-Fe}}$. (**B**) The current map $I(\vec{\mathbf{r}},E = +50\ \text{meV})$ in the same FOV as (A). (Inset) Autocorrelation analysis of this image; the centers of self-similarity peaks (red dotted lines) are separated by ~$8a_{\text{Fe-Fe}}$. (**C**) The current map $I(\vec{\mathbf{r}},E = +50\ \text{meV})$ in the same FOV as in (A) and (B). The atomic-scale impurity state locations as determined from conductance mapping at 150 meV are shown as 262 yellow dots. If they represent the Co dopant atoms, they exhibit only ~15% of the density expected in the top FeAs layer, based on the average measured Co density of the whole sample. (Inset) A typical conductance spectrum exhibits a mixed metallic and "pseudogap-like" shape.

states $DOS(E = 0)$ with a V-shaped "pseudogap" spectrum superimposed. The cobalt dopant-atom locations should, in theory (*35*), be detectable as atomic-scale local conductance maxima between +100 and +200 meV. The locations of atomic-scale impurity states imaged in this energy range are shown in Fig. 2C as yellow dots overlaid on the same $I(\vec{\mathbf{r}}, E = 50\ \text{meV})$ map; the normalized cross-correlation between this I map and dopant locations can be as high as 0.22. Thus, some degree of dopant-atom pinning of the unidirectional static electronic nanostructure seems to be occurring.

From these data, static, self-similar, electronic nanostructures of dimension ~$8a_{\text{Fe-Fe}}$ that are aligned in a unidirectional fashion along the a axis (AF axis) and correlated in their locations with dopant atoms appear to exist in underdoped $Ca(Fe_{1-x}Co_x)_2As_2$. If this is correct, the $\vec{\mathbf{k}}$-space electronic structure should exhibit (i) C_2 symmetry with dispersive excitations along the b axis and (ii) a $\vec{\mathbf{q}} \doteq 2\pi/8a_{\text{Fe-Fe}}$ band folding along the a axis. To test this picture, we determine the simultaneous $\vec{\mathbf{k}}$-space electronic structure through quasiparticle interference (QPI) imaging. Important to the demonstration of ferropnictide QPI here was the development of large-FOV, flat, stable surfaces of $Ca(Fe_{1-x}Co_x)_2As_2$. In fig. S4 (*36*), we show the unprocessed $g(\vec{\mathbf{r}}, E)$ data measured in a 40-nm square FOV of such a surface, over an energy range from $E = -20$ to +25 meV. The wavelength of conductance modulations is long and increases continuously with increasing energy, but only along the vertical axis of these images (*36*). The resulting $g(\vec{\mathbf{q}}, E)$ are shown in Fig. 3, A to J, and figs. S4 and S5. Their dispersion is seen in the evolution between Fig. 3, A and J; it evolves along one axis only. This means that the scattering interference modulations are strongly unidirectional, which should occur if the $\vec{\mathbf{k}}$-space band supporting them is nematic. Finally, not one, but three parallel sets of dispersive peaks exist in all of these QPI data (e.g., vertical arrows below Fig. 3J).

To further analyze these data, we consider the relative orientation of the dispersive QPI modulations to the crystal axes (Fig. 3K). The QPI modulations are at 45° to the surface reconstruction and exhibit $\vec{\mathbf{q}}$-vector magnitudes smaller than those of any crystal or surface periodicity; thus, these QPI signals are not influenced by the surface reconstruction. In Fig. 3L, we show that the three sets of $\vec{\mathbf{q}}$ vectors disperse on $\vec{\mathbf{q}}(E)$ trajectories identical to each other up to a displacement by $\vec{\mathbf{q}} \doteq \pm 2\pi/8a_{\text{Fe-Fe}}$. This is what would be expected from a band folding due to a ~$8a_{\text{Fe-Fe}}$ periodic reconstruction of the $\vec{\mathbf{r}}$-space electronic structure along the a axis.

The ARPES-measured dispersion of the α_2 band (*34*) is shown in fig. S6 (*36*). When the $\vec{\mathbf{k}} = \pm\vec{\mathbf{q}}/2$ (here, $\vec{\mathbf{k}}$ is a momentum-space wave vector) points taken from QPI data in Fig. 3L are overlaid centered on its Γ point (Γ is at the center of the Brillouin zone), they appear to be in good agreement. Thus, the observed QPI data are consistent with scattering between states in the α_2 band, but a version of this band actually exhibits C_2 symmetry plus an additional $\vec{\mathbf{q}} \doteq \pm 2\pi/8a_{\text{Fe-Fe}}$ folding.

A final test of the validity of this emerging picture of static, a-axis–oriented, ~$8a_{\text{Fe-Fe}}$ electronic nanostructures generating a C_2-symmetric,

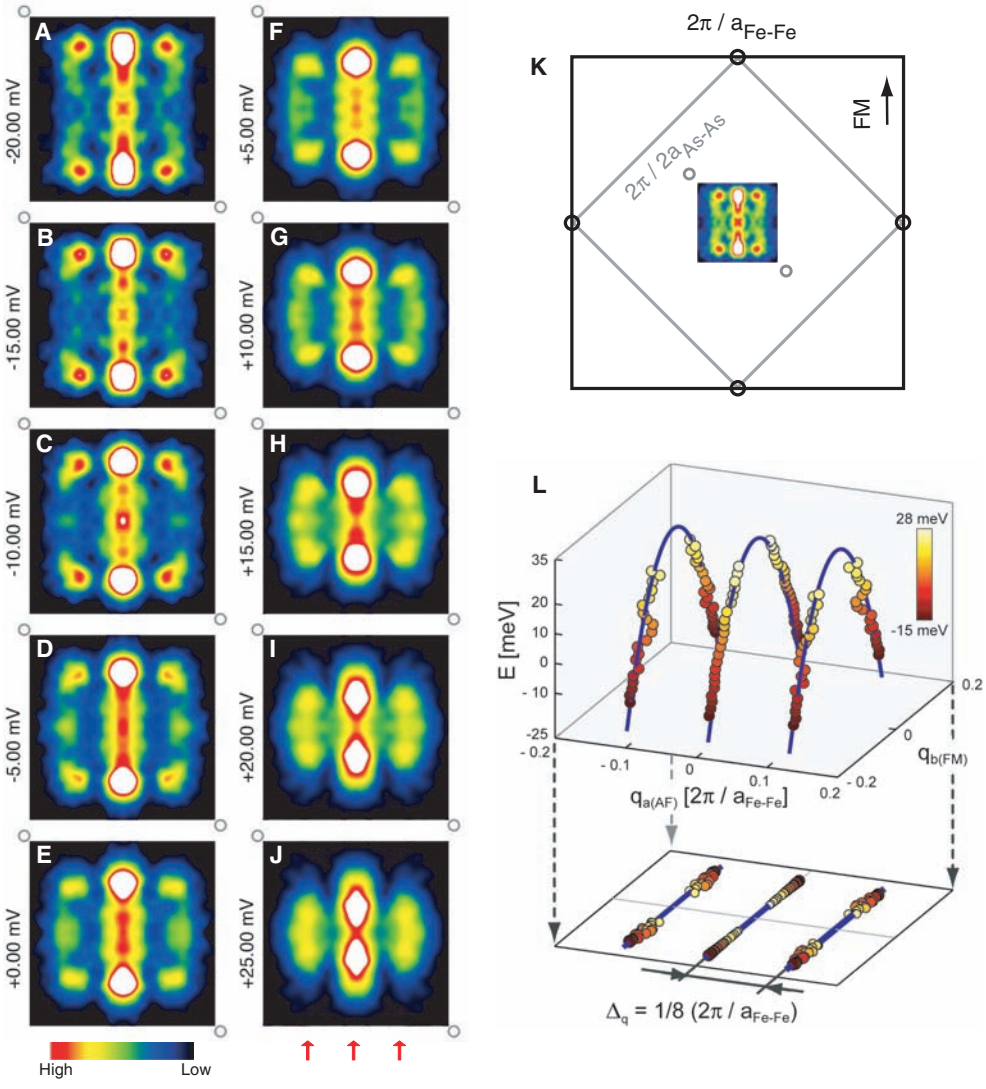

Fig. 3. (**A** to **J**) The Fourier transforms $g(\vec{\mathbf{q}}, E)$ of the $g(\vec{\mathbf{r}}, E)$ images in fig. S4 reveal the highly C_2-symmetric structure of the QPI patterns. The data shown here are from a larger 94-nm square FOV. Six dispersing peaks are clearly visible. The two center peaks disperse in a hole-like fashion along the b axis only. Pairs of side peaks mimic their dispersion at $\vec{\mathbf{q}} \approx \pm 1/8(2\pi/a_{\text{Fe-Fe}})$. The open circles at two corners of each image represent the $\vec{\mathbf{q}}$-space locations of the 1 × 2 reconstruction. Red arrows indicate the three parallel dispersion trajectories. (**K**) Overview of the different directions and length scales in $\vec{\mathbf{q}}$ space. The dispersing QPI vectors are short compared with the $2\pi/a_{\text{Fe-Fe}}$ box that spans all scattering vectors in the first Fe-Fe Brillouin zone (the large black box). The small gray box indicates the first As-As reciprocal unit cell. FM indicates the b axis direction along which spin correlations are ferromagnetic. (**L**) The hole-like dispersion of QPI, plotted in $\vec{\mathbf{q}}_b, \vec{\mathbf{q}}_a, E$ space. Circles mark the positions of the six dispersion peaks extracted from each $g(\vec{\mathbf{q}}, E)$ image; the blue lines are the parabolic fit for QPI. Projections to the $(\vec{\mathbf{q}}_b, \vec{\mathbf{q}}_a)$ plane emphasize how unidirectional the dispersions are along the b axis. The side peaks are at ~$\pm 1/8(2\pi/a_{\text{Fe-Fe}})$, suggesting an intimate relation between the unidirectional QPI modulations and unidirectional static electronic structure in Fig. 2.

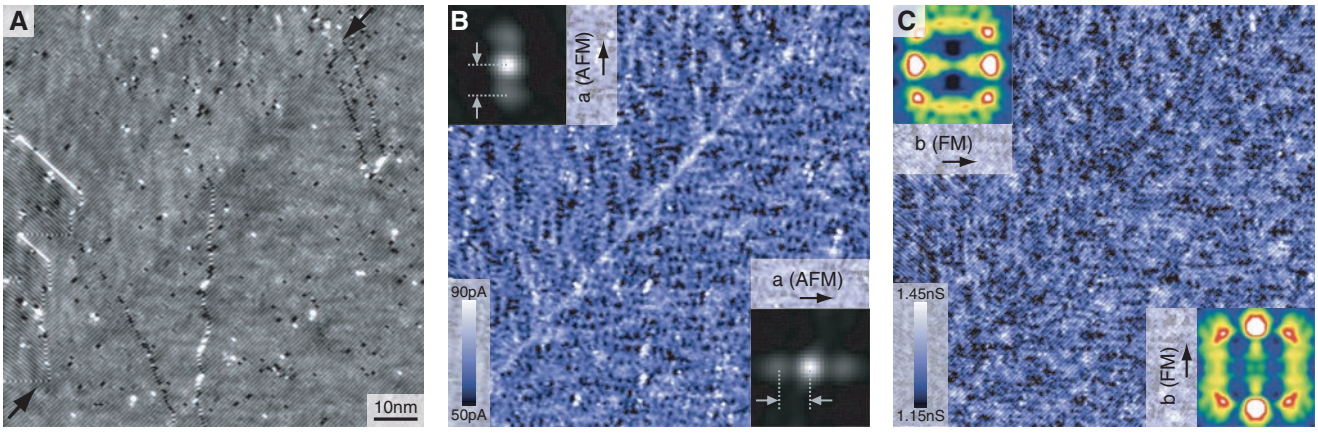

Fig. 4. (**A**) A 96.0-nm FOV topographic image (junction resistance = 500 megohm, $V_0 = -50$ mV) measured simultaneously with the $g(\vec{\mathbf{r}},E)$ and $I(\vec{\mathbf{r}},E)$ data of (B) and (C). The orthorhombic twin boundary visible in (B) and (C) is marked with black arrows. Slight deviations in the angle of the surface-reconstruction reveal the orthogonal orthorhombic axes of the two crystal domains (*36*). (**B**) The current image, $I(\vec{\mathbf{r}},E = 50\ \text{meV})$ in the same FOV as (A). The static unidirectional domains of Fig. 2 clearly change directionality by 90° across the twin boundary. (Insets) Autocorrelations; center of self-similarity peaks (gray dotted lines) are separated by ~$8a_{\text{Fe-Fe}}$. (**C**) The conductance image $g(\vec{\mathbf{r}},E = -10\ \text{meV})$ in the same FOV. (Insets) Fourier-transforms in the respective domains demonstrate that the QPI dispersions exhibit a 90° rotation across the twin boundary.

quasi-folded band along the *b* axis would be to detect the effect of an orthorhombic twin boundary. In Fig. 4A, we show a 96-nm square topograph through which a twin boundary passes diagonally (*36*). Figure 4B depicts the *I* map taken simultaneously with Fig. 4A, along with the autocorrelations of this map on each side of the twin boundary. In both the raw data and the autocorrelations, the static ~$8a_{\text{Fe-Fe}}$ *a*-axis–oriented domains rotate through 90°. In Fig. 4C, we show the $g(\vec{\mathbf{r}},E = -10\ \text{meV})$ taken simultaneously along with the two $g(\vec{\mathbf{q}},E = -10\ \text{meV})$ measured on each side of the twin boundary. Again, the C_2-symmetric *b* axis QPI modulations rotate through 90°. This rules out effects of both the surface reconstruction and the distribution of Ca atoms remaining on that surface (neither of which rotates at the twin boundary) as the cause of the observed electronic nematicity. Instead, we conclude that all the unidirectional electronic phenomena (both in $\vec{\mathbf{r}}$ space and $\vec{\mathbf{k}}$ space) detected here are bulk electronic characteristics of the orthorhombic antiferromagnetic state. Hence, a related conclusion is that C_4-symmetric photoemission data in this state must represent the average over a strongly C_2-symmetric electronic structure in different orthorhombic domains.

Our SI-STM studies indicate that the electronic structure of underdoped $Ca(Fe_{1-x}Co_x)_2As_2$ supports a variety of unexpected phenomena, including (i) the existence of unidirectional electronic nanostructures, which are highly self-similar with dimension ~$8a_{\text{Fe-Fe}}$ and possibly pinned by Co dopant atoms, and (ii) *b*-axis dispersive QPI modulations, consistent with a nematic version of the α_2 band and with an additional apparent $\vec{\mathbf{q}} \doteq \pm 2\pi/8a_{\text{Fe-Fe}}$ band folding. As none of these effects are expected merely due to the crystal symmetry, the underdoped ferropnictide parent state from which superconductivity emerges appears to be a more complex electronic nematic than originally expected. These new perceptions of its electronic structure should inform revised theories for the mechanism of the high-temperature superconductivity.

References and Notes

1. Y. Kamihara, T. Watanabe, M. Hirano, H. Hosono, *J. Am. Chem. Soc.* **130**, 3296 (2008).
2. X. H. Chen *et al.*, *Nature* **453**, 761 (2008).
3. C. Wang *et al.*, *Europhys. Lett.* **83**, 67006 (2008).
4. M. Rotter, M. Tegel, D. Johrendt, *Phys. Rev. Lett.* **101**, 107006 (2008).
5. A. S. Sefat *et al.*, *Phys. Rev. Lett.* **101**, 117004 (2008).
6. N. Ni *et al.*, *Phys. Rev. B* **78**, 014523 (2008).
7. J. Zaanen, O. Gunnarsson, *Phys. Rev. B* **40**, 7391 (1989).
8. S. A. Kivelson, E. Fradkin, V. J. Emery, *Nature* **393**, 550 (1998).
9. S. Sachdev, *Rev. Mod. Phys.* **75**, 913 (2003).
10. V. J. Emery, S. A. Kivelson, J. M. Tranquada, *Proc. Natl. Acad. Sci. U.S.A.* **96**, 8814 (1999).
11. Y. Kohsaka *et al.*, *Science* **315**, 1380 (2007); published online 7 February 2007 (10.1126/science.1138584).
12. Y. Kohsaka *et al.*, *Nature* **454**, 1072 (2008).
13. H. Hosono, *Physica C* **469**, 314 (2009).
14. J. Zhao *et al.*, *Nat. Phys.* **5**, 555 (2009).
15. S. O. Diallo *et al.*, *Phys. Rev. Lett.* **102**, 187206 (2009).
16. T. Yildirim, *Phys. Rev. Lett.* **101**, 057010 (2008).
17. Q. Si, E. Abrahams, *Phys. Rev. Lett.* **101**, 076401 (2008).
18. C. Fang, H. Yao, W.-F. Tsai, J. Hu, S. A. Kivelson, *Phys. Rev. B* **77**, 224509 (2008).
19. I. I. Mazin, M. D. Johannes, *Nat. Phys.* **5**, 141 (2009).
20. C. Xu, Y. Qi, S. Sachdev, *Phys. Rev. B* **78**, 134507 (2008).
21. H. Zhai, F. Wang, D.-H. Lee, *Phys. Rev. B* **80**, 064517 (2009).
22. F. Krüger, S. Kumar, J. Zaanen, J. van den Brink, *Phys. Rev. B* **79**, 054504 (2009).
23. R. R. P. Singh, http://arxiv.org/abs/0903.4408 (2009).
24. C.-C. Lee, W.-G. Yin, W. Ku, http://arxiv.org/abs/0905.2957 (2009).
25. W.-C. Lee, C. Wu, *Phys. Rev. Lett.* **103**, 176101 (2009).
26. Y. Yin *et al.*, *Phys. Rev. Lett.* **102**, 097002 (2009).
27. M. C. Boyer *et al.*, http://arxiv.org/abs/0806.4400 (2008).
28. F. Massee *et al.*, *Phys. Rev. B* **79**, 220517 (2009).
29. D. Hsieh *et al.*, http://arxiv.org/abs/0812.2289 (2008).
30. V. B. Nascimento *et al.*, *Phys. Rev. Lett.* **103**, 076104 (2009).
31. F. C. Niestemski *et al.*, http://arxiv.org/abs/0906.2761 (2009).
32. A. I. Goldman *et al.*, *Phys. Rev. B* **78**, 100506 (2008).
33. S.-H. Baek *et al.*, *Phys. Rev. B* **79**, 052504 (2009).
34. T. Kondo *et al.*, http://arxiv.org/abs/0905.0271 (2009).
35. A. F. Kemper, C. Cao, P. J. Hirschfeld, H.-P. Cheng, *Phys. Rev. B* **80**, 104511 (2009).
36. Materials and methods are available as supporting material on *Science* Online.

37. We thank F. Baumberger, P. J. Hirschfeld, J. E. Hoffman, A. Kaminski, D.-H. Lee, G. Luke, E.-A. Kim, M. Lawler, A. P. Mackenzie, I. I. Mazin, M. Norman, S. Pan, G. Sawatzky, and S. Uchida for helpful discussions and communications. These studies are supported by the Center for Emergent Superconductivity, a DOE Energy Frontier Research Center headquartered at Brookhaven National Laboratory. Work at the Ames Laboratory was supported by the DOE, Basic Energy Sciences under Contract no. DE-AC02-07CH11358. Support for this work was provided by NSF/DMR-0654118 through the National High Magnetic Field Lab (to T.-M.C.); the Cornell Center for Materials Research under NSF/DMR-0520404 (to Y.X.); and the U.K. Engineering and Physical Sciences Research Council and the Scottish Funding Council (to M.P.A.). J.C.D. acknowledges gratefully the hospitality and support of the Physics and Astronomy Department at the University of British Columbia, Vancouver, BC, Canada.

Supporting Online Material

www.sciencemag.org/cgi/content/full/327/5962/181/DC1
Materials and Methods
SOM Text
Figs. S1 to S7
References

25 August 2009; accepted 13 November 2009
10.1126/science.1181083